ACS APPLIED MATERIALS & INTERFACES

Research Article

www.acsami.org

Comparative Electrochemical Analysis of Crystalline and Amorphous Anodized Iron Oxide Nanotube Layers as Negative Electrode for LIB

Syed Atif Pervez,[†,‡] Doohun Kim,[‡,*] Umer Farooq,[†,‡] Adnan Yaqub,[†,‡] Jung-Hee Choi,[‡] You-Jin Lee,[‡] and Chil-Hoon Doh[†,‡]

[†]Korea Electro-technology Research Institute (KERI), Changwon 642-120, Republic of Korea

[‡]Electrical Functionality Material Engineering (KERI Campus), Korea University of Science and Technology, Daejeon 305-333, Republic of Korea

Supporting Information

ABSTRACT: This work is a comparative study of the electrochemical performance of crystalline and amorphous anodic iron oxide nanotube layers. These nanotube layers were grown directly on top of an iron current collector with a vertical orientation via a simple one-step synthesis. The crystalline structures were obtained by heat treating the as-prepared (amorphous) iron oxide nanotube layers in ambient air environment. A detailed morphological and compositional characterization of the resultant materials was performed via transmission electron microscopy (TEM), field-emission scanning electron microscopy (FE-SEM), X-ray diffraction (XRD), and Raman spectroscopy. The XRD patterns were further analyzed using Rietveld refinements to gain in-depth information on their quantitative phase and crystal structures after heat treatment. The results demonstrated that the crystalline iron oxide nanotube layers exhibit better electrochemical properties than the amorphous iron oxide nanotube layers when evaluated in terms of the areal capacity, rate capability, and cycling performance. Such an improved electrochemical response was attributed to the morphology and three-dimensional framework of the crystalline nanotube layers offering short, multidirectional transport lengths, which favor rapid Li^+ ions diffusivity and electron transport.

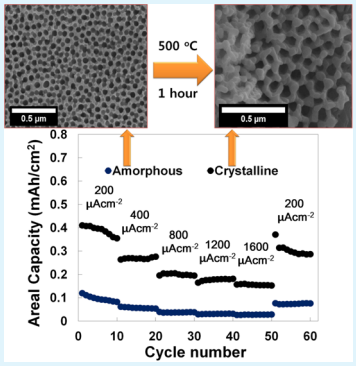

KEYWORDS: *nanotube layers, comparative analysis, anodization, battery*

INTRODUCTION

Li-ion batteries (LIBs) have been widely studied as electrochemical energy storage devices with high energy and power density, because of their enormous potential to power electric vehicles and portable electronic devices.[1−3] The current commercial LIB industry predominantly utilizes graphite as the anode material.[4,5] Although graphite has shown good electrochemical performance over the years, the ever-increasing energy demands of the industry has opened the scope to explore other materials for the LIB anode. Transition metal oxides (TMOs) are considered suitable replacements for graphite due to their higher specific capacity, widespread availability, and better safety features.[6−9] The higher capacity obtained for TMOs is principally based on the reversible redox reaction between lithium and the transition metal cations. To make this redox reaction more efficient and reversible, the material dimensions are reduced to the nanoscale range via proper design and engineering.[9−12]

Of the various synthetic techniques for nanostructured TMOs,[13−19] electrochemical anodization[20,21] is of particular interest because it is comparatively inexpensive and simply provides self-aligned nanostructures over a large surface area. Recently, significant interest has developed in utilizing TMO nanotube layers (NTs) grown via anodization as the LIB anode. Ortiz and co-workers[6,22] used anodized TiO_2 NTs as the anode in a battery application for the first time. Such a structure is particularly advantageous for battery performance because the vertical alignment of the nanotubes offers enhanced kinetics for the vectorial charge/electron transfers. Additionally, directly growing the oxide layers on top of the metal current collector avoids the need for a binder and conductive additives in the structure, which simplifies the synthesis and stabilizes the material. Although promising results have been demonstrated using TiO_2 NTs,[22−26] the inherently low theoretical capacity of TiO_2 (168 mAh/g for $Li_{0.5}TiO_2$) is a major concern for achieving high energy densities. Therefore, TiO_2 must be replaced with another material with a higher theoretical capacity. Iron oxide is a potential candidate to replace TiO_2 due to the high theoretical capacity of its crystalline phase (1007 mAh/g for hematite and 926 mAh/g for magnetite).[7,8,27,28] When structured as NTs grown on top of the iron (Fe) current collector, iron oxide is expected to exhibit excellent electrochemical performance. Recently, several studies have reported the synthesis and application of iron oxide NTs as battery anodes.[21,29] These reports have mainly focused on either the surface modification of the nanotubes or making

Received: March 7, 2014
Accepted: June 25, 2014
Published: June 25, 2014

composites with other materials. Because the iron oxide crystalline phases are better suited to battery performance due to their high theoretical capacities, analyzing their electrochemical response relative to the respective amorphous phases is important especially when they are grown through anodization. However, to the best of our knowledge, no reports have specifically focused on the electrochemical behaviors of crystalline iron oxide NTs relative to their amorphous phase while retaining the same structural morphology.

Herein, highly ordered crystalline and amorphous anodic iron oxide NTs with high aspect ratios undergo a detailed comparative analysis. The NTs are directly grown on the Fe foil without any binder or conductive additives and are further heat treated to obtain the hematite/magnetite crystalline phase. The heat treatment conditions (time, temperature, and environment) were optimized to retain the anodized structure morphology after annealing. Transmission electron microscopy (TEM), field-emission scanning electron microscopy (FE-SEM), X-ray diffraction (XRD), Raman spectroscopy, and Rietveld analyses were used to morphologically and compositionally characterize the material, while the electrochemical responses were examined via cyclic voltammetry (CV) and charge−discharge cycling. The results indicated a superior electrochemical response for the crystalline iron oxide NTs relative to the amorphous ones in terms of their areal capacity, rate capability, and cycling performance. The improved crystallinity, having a three-dimensional hematite/magnetite phase framework, and traits unique to the anodized structure were responsible for this enhanced performance.

EXPERIMENTAL SECTION

Material Synthesis. Fe foils (0.1 mm thickness, 99.99% purity, Nilaco Japan) cut into 1.5 cm^2 squares were degreased by sonicating in acetone and then ethanol for 20 min each. The electrochemical anodization technique was performed to synthesize the iron oxide NTs using a DC-voltage potentiostat (OPS-22101, ODA, Korea) by applying a constant 40 V for 60 min.[30] An Fe foil was used as the working electrode, while a platinum mesh served as the counter electrode. The electrolyte solution was a mixture of 0.1 M NH_4F, 1 M H_2O, and ethylene glycol. A water circulating heater was used during these experiments to maintain a bath temperature of 20 °C for the electrolyte. After anodization, the samples were initially stored overnight in ethanol, rinsed, and finally dried in an oven. The amorphous samples were heat treated in a furnace at 500 °C for 1 h under ambient air to obtain the hematite/magnetite crystalline phase of the material using a furnace (XY-1400S, Hantech, Korea) with a heating and cooling rate of 10 °C/min.

Material Characterization. The NT morphology was determined via FE-SEM (Hitachi S4800). The TEM images and selected area electron diffraction (SAED) patterns were obtained via transmission electron microscope (Philips TF30ST). To prepare the TEM samples, the oxide layer was scratched from the Fe foil surface and dispersed onto a carbon grid. The crystallinity of the corresponding material phases was confirmed via XRD analysis using an X-ray diffractometer (Philips X'pert-MPD) with a Panalytical X'celerator detector with graphite monochromized Cu Kα radiation (λ = 1.54056 Å). The Raman spectra were obtained using a Raman spectrometer (NTEGRA SPECTRA NT, MDT) with a laser excitation wavelength of 532 nm.

Electrochemical Measurements. Coin half-cells were assembled in a dry room to evaluate the electrochemical performance of the material. Iron oxide NTs grown on top of the Fe current collector served as the working electrode with a polypropylene membrane (Celgard 2325, Celgard, Inc.) as a separator and Li-metal (purity 99.9%) as the counter electrode. The electrolyte was 1.2 M $LiPF_6$ in EC/DMC (1:1, v/v). The assembled cells had an open circuit voltage of approximately 3 V and were galvanostatically charged/discharged at current densities ranging from 100 to 1600 μA cm^{-2} across the potential range from 0.005 to 3 V using a multichannel battery tester (TOYO TOSCAT-3100U). The CV analyses were performed via an electrochemical setup (model VMP3, Bio Logic, France) with a 0.1 mV/s scan rate across the voltage range from 0.005 to 3 V.

RESULTS AND DISCUSSION

Figure 1a−c shows the FE-SEM images for iron oxide NTs grown via electrochemical anodization. A two-step anodization

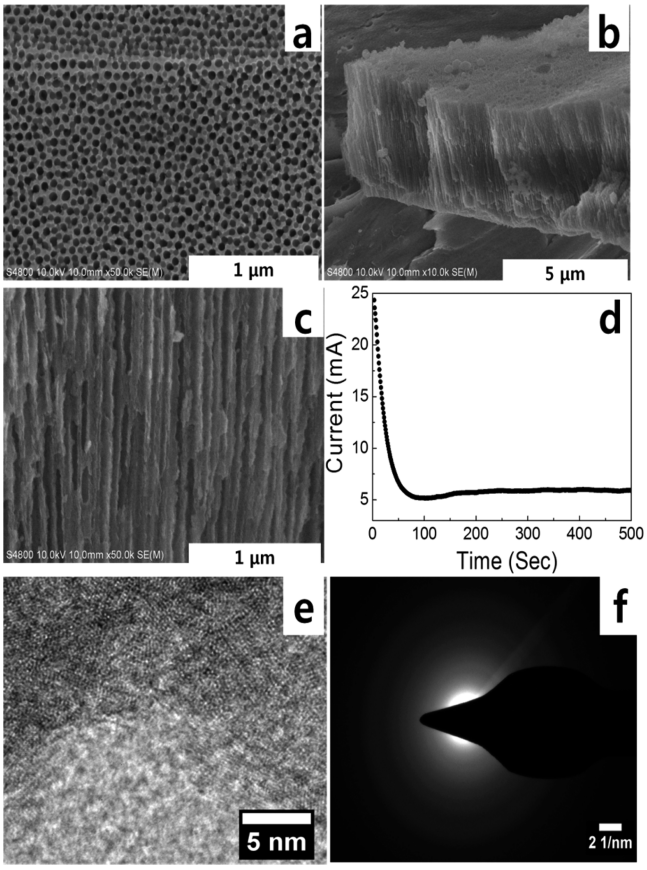

Figure 1. SEM and TEM images of the amorphous iron oxide NTs formed via anodization. (a) Surface morphology and (b, c) cross-sectional views with different magnifications. (d) Current−time transient curve for the anodization process. (e) HR-TEM image for a portion of the nanotube. (f) SAED pattern.

process[31,32] was adopted to grow morphologically suitable nanotubes. A series of anodization experiments were conducted to determine the best NT morphology as shown in Figure S1 in the Supporting Information. The anodization temperature and time significantly impacted the nanotube structure as mentioned by Roy et al. for other metal oxides.[20] The optimized anodization conditions were 40 V for 1 h at 20 °C, which yielded a tube length of approximately 5 μm with a pore diameter of approximately 60 nm. Figure 1 indicates a high porosity, length, and vertical directionality were successfully achieved. Such structural traits are well suited for the rapid diffusion of the electrolyte within the pores with a high electrode surface area and fast Li^+ ion/electron transport kinetics. Figure 1d shows the typical current−time curve associated with the growth. A close analysis of the transient curve indicates the iron oxide NT growth mechanism resembles that of the anodized TiO_2 nanotubes.[20,33,34] An abrupt fall in

the current was initially observed due to the formation of a compact oxide layer on the metal surface. Soon afterward, the current begins to increase due to the etching of this surface oxide layer by the fluoride ions. However, the current eventually levels off, which indicates a balance between the formation and etching of the oxide layer and hence a regular NT formation. The HR-TEM lattice image of the as-prepared sample shown in Figure 1e indicates the lack of a proper crystal structure, which implies an amorphous material. This result was confirmed by the SAED patterns shown in Figure 1f, which had no clear evidence of any diffraction rings.

To obtain crystalline iron oxide NTs, the as-prepared samples were heated to 500 °C for 1 h under ambient air. For the material characterization, the XRD patterns of both the amorphous and crystalline samples were obtained and refined using the Rietveld calculations as shown in Figure 2a and b.

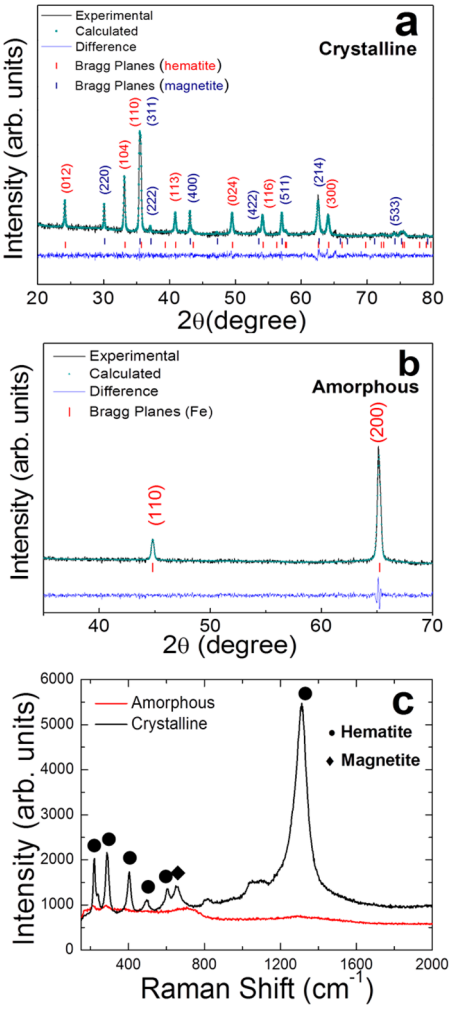

Figure 2. Rietveld refined XRD results (a, b) and Raman spectral analyses (c) for the crystalline and amorphous samples.

The Rietveld analysis was performed to quantify the phase and crystal structure using the GSAS package.[35] The figures clearly show the diffraction peaks corresponding to hematite and magnetite phases of iron oxide appearing upon heat treatment. This analysis was also supported by the energy dispersive X-ray spectrum (Supporting Information Figure S2), where O and Fe are the major elements with O almost doubling the atomic percentage of Fe. Contrary to the crystalline samples, the amorphous samples showed no diffraction peaks for the oxide layer other than the prominent Fe substrate peaks, which confirms their amorphous nature. These results agree with previously reported works.[30,36] The lattice parameters calculated via Rietveld refinement for the hematite phase are a, b = 5.02 Å and c = 13.71 Å, which confirms a hexagonal crystal structure consistent with the literature values (JCPDS card no. 33-0664) and indexed according to the $R\bar{3}c$ space group. Similarly, the magnetite phase had a, b, c = 8.37 Å, which is a cubic crystal structure consistent with literature values (JCPDS card no. 01-1111) and indexed according to the $Fd\bar{3}m$ space group. The unit cell diagrams for the hexagonal hematite and cubic magnetite are shown in Figure S3 in the Supporting Information. To further confirm the hematite/magnetite phases in the heat treated sample, Raman spectroscopy was performed for the crystalline and amorphous NTs, as shown in Figure 2c. Relative to the amorphous NTs, the crystalline NTs contained clear Raman modes corresponding to the hematite phase with traces of magnetite.

Although an improved crystallinity is advantageous to the electrochemical performance of the electrode, as will be shown shortly, it should not be achieved at the expense of the unique NT morphology, which provides the many advantages detailed earlier. The heat treatment can easily destroy the nanotube morphology;[37] therefore, the annealing time, temperature, and furnace environment must be optimized.

Figure 3 shows the FE-SEM and HR-TEM images of the NTs after the optimized heat treatment under an ambient

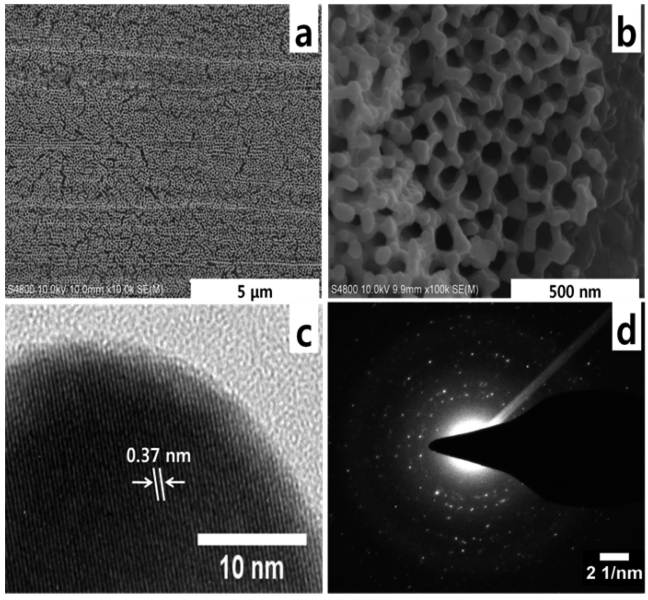

Figure 3. SEM and TEM images of the crystalline iron oxide NTs: (a, b) Surface morphology with different magnifications. (c) HR-TEM image of a portion of nanotube. (d) SAED pattern.

environment. A color change from brown to black was observed by the naked eye for the oxide layer after the heat treatment as shown in Figure S4 in the Supporting Information. Figure 3a and b shows the surface NT morphologies at different magnification after heat treatment. When compared to Figure 1, the NT surface morphologies were well retained. Closer inspection (Figure 3b) revealed the tube diameter had increased to approximately 80 nm, and its shape has transformed from roundish to more hexagonal. Such a change

in the tube structure was possibly due to the initiation layer removal post annealing. The initiation layer is an oxide layer remnant frequently found on top of the tubes after anodization that covers the ordered oxide layers.[20,38,39] Such remnant layers are undesirable because they hamper the tube transport properties as the proper NT geometry is not exposed to the lithiation/delithiation process during battery operation. The improved material crystallinity is further evident from the HR-TEM and SAED pattern images shown in Figure 3c and d. Contrary to Figure 1e and f, clear lattice fringes and bright diffraction rings were observed. The crystal lattice spacing was measured as 0.37 nm, which agrees well with the *d*-spacing of the (012) plane in hematite iron oxide

The electrochemical responses in terms of the Li^+ intercalation and deintercalation during the first three charge/discharge cycles for both the crystalline and amorphous samples are presented in Figure 4. The current density was

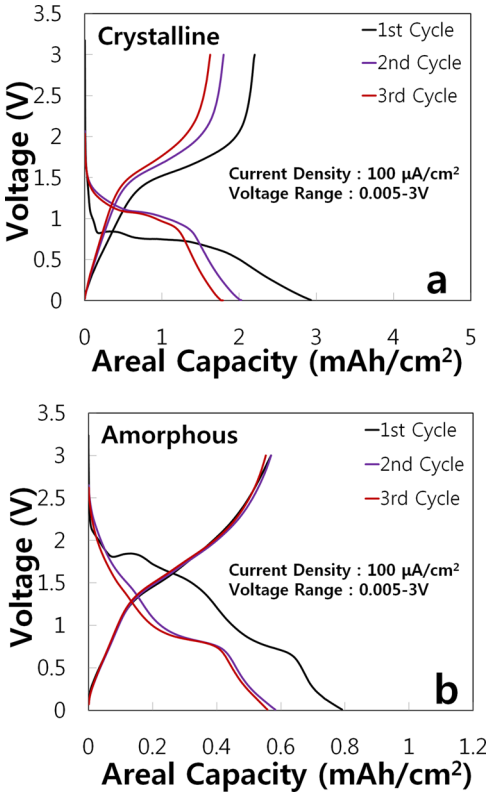

Figure 4. Initial galvanostatic charge/discharge curves for (a) crystalline and (b) amorphous iron oxide NTs between 0.005 and 3 V at a current density of 100 $\mu A/cm^2$.

100 $\mu A/cm^2$, while the voltage range was between 0.005 and 3.0 V. The areal capacity was calculated by considering the active surface area of 1.13 cm^2 of the anodized iron oxide layer. For the crystalline NTs during the first discharge cycle, the voltage plateaued at approximately 0.9 V, which was maintained to provide a high areal capacity (2.9 mAh/cm^2). During the second and third discharge cycles, the voltage plateau shifted from 0.9 V to approximately 1.2 V. In contrast to the crystalline samples, no well-defined voltage plateau was observed for the amorphous samples during the first cycle, which was mainly due to their lack of order and the presence of random defects. Additionally, the first discharge capacity (0.79 mAh/cm^2) was significantly lower than that for the crystalline samples. The higher areal capacity of the crystalline NTs was attributed to their hexagonal/cubic structure containing many open and ordered three-dimensional channels that facilitate the insertion/extraction of Li^+ ions during charge/discharge (Supporting Information Figure S3). Furthermore, their better morphology and crystallinity enhance the electron transport, which contributes to their higher capacity.

Figure 5a shows the rate capability tests for the crystalline and amorphous NTs using current densities ranging from 200

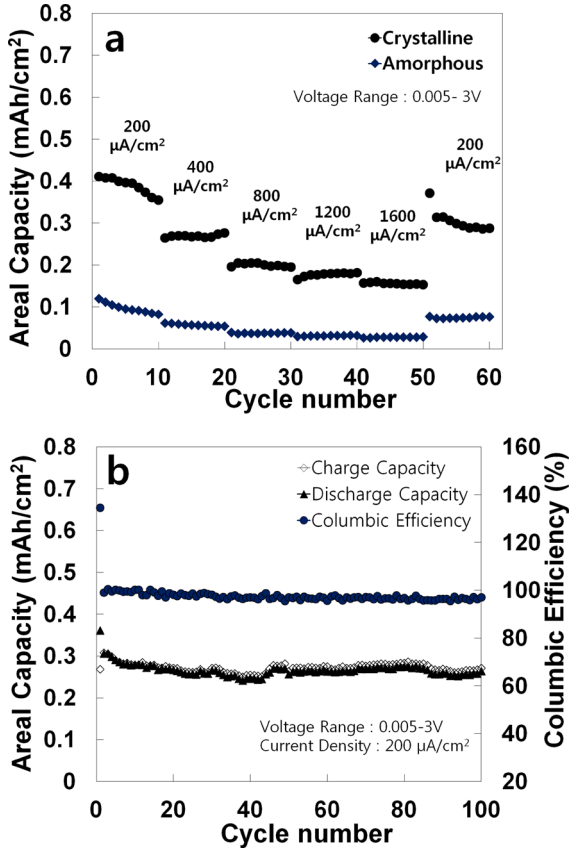

Figure 5. (a) Comparative rate capability tests for crystalline and amorphous iron oxide NTs evaluated at various current densities from 200 to 1600 $\mu A/cm^2$. (b) Cyclic performance and columbic efficiency for the crystalline NTs obtained at a current density of 200 $\mu A/cm^2$ immediately after the rate capability test.

to 1600 $\mu A/cm^2$. Prior to the rate ability test, the electrodes were cycled at 100 $\mu A/cm^2$ for 15 cycles for a stable formation of the SEI layer. From the figure it is evident that compared to the amorphous NTs the crystalline NTs exhibited superior rate capabilities. The crystalline NTs exhibited capacities of approximately 0.40 mAh/cm^2 at a current density of 200 $\mu A/cm^2$ and approximately 0.155 mAh/cm^2 at 1600 $\mu A/cm^2$. These values were significantly higher than those of the amorphous NTs, that is, 0.10 mAh/cm^2 at 200 $\mu A/cm^2$ and 0.02 mAh/cm^2 at 1600 $\mu A/cm^2$. Additionally, the capacity recovery of the crystalline NTs was approximately 90% when the current density is reduced from 1600 to 200 $\mu A/cm^2$, which indicates a swift response and good stability for the material at various current densities.

To evaluate the capacity retention for the crystalline iron oxide NTs, cyclic performance tests were performed immediately after the rate capability tests. The results are quite remarkable and are shown in Figure 5b. For a current density of

200 μA/cm^2, a capacity of approximately 280 μAh/cm^2 was retained over 100 cycles. Additionally, the charge/discharge capacity reversibility was good with an average 98% columbic efficiency. Such a performance demonstrates the excellent stability and integrity of the electrode material even after cycling repeatedly at various current densities.

A CV analysis was performed to compare the Li^+ intercalation reversibility and kinetics for both the amorphous and crystalline iron oxide NTs. Figure 6 shows the 1st, 5th, and

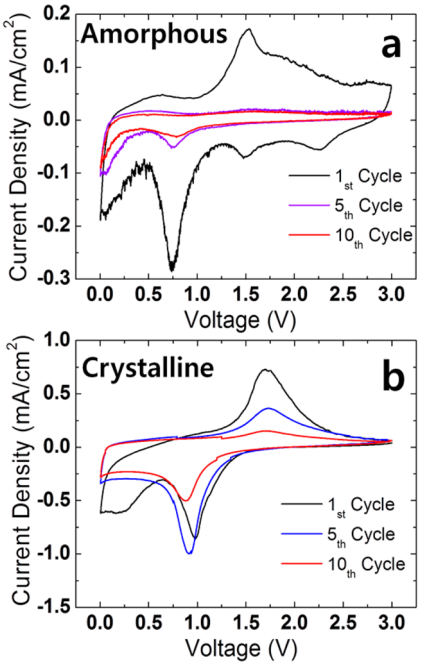

Figure 6. 1st, 5th, and 10th CV cycles for the (a) amorphous and (b) crystalline iron oxide NTs using a scan rate of 0.1 mV/s across the potential range from 0.005 to 3 V (vs Li/Li$^+$).

10th CV cycles for both types of NTs using a scan rate of 0.1 mV/s across the potential range from 0.005 to 3 V vs Li/Li$^+$. During the first cathodic scan, the strong reduction peaks at 0.75 V for the amorphous NTs and 1 V for the crystalline NTs were attributed to the conversion from Fe^{3+} to Fe^0, while the additional peaks corresponded to Li^+ intercalated into the structure.[40] In the anodic scan, no additional peaks were observed except for a single prominent oxidation peak at 1.5 and 1.7 V for the amorphous and crystalline NTs, respectively. These peaks account for the oxidation from Fe^0 to Fe^{3+}. This mechanism follows the chemical reaction given below:

$$Fe_2O_3 + 6Li^+ + 6e^- \leftrightarrow 2Fe^0 + 3Li_2O$$

The oxidation/reduction peak intensities were significantly reduced for the amorphous NTs during the 5th and 10th CV cycles. However, the crystalline NTs maintained well-defined cathodic and anodic peaks with high intensities and constant redox potentials. Such behavior clearly shows the Li^+ insertion/desertion redox reactions are more active in the crystalline structure. The plot also shows that the area under the current density−voltage curve was significantly larger for the crystalline structure than the amorphous structure. This result further supports the argument made in Figure 4 about the increased capacity from the improved crystallinity in the crystalline iron oxide NTs.

CONCLUSIONS

In summary, a detailed comparison between the electrochemical responses for crystalline and amorphous anodic iron oxide NTs used as the battery anode was performed. Oxide layers with well-defined morphologies and high aspect ratios were initially grown and then heat treated to convert into the crystalline phase. A comprehensive morphological and compositional characterization was performed for both the amorphous and crystalline samples to confirm their crystallinity and structure. The results demonstrated the superior electrochemical performance of crystalline iron oxide NTs over amorphous NTs in terms of their areal capacity, rate capability, and cycling performance. A suitable morphology and improved crystallinity are the main material characteristics responsible for this enhanced performance.

ASSOCIATED CONTENT

Supporting Information

Additional SEM images, EDS spectra with their quantitative results, material unit cell diagrams, and digital images of the samples both before and after heat treatment. This material is available free of charge via the Internet at http://pubs.acs.org.

AUTHOR INFORMATION

Corresponding Author

*E-mail: kdh0121@keri.re.kr.

Notes

The authors declare no competing financial interest.

ACKNOWLEDGMENTS

This study was supported by Korea Research Council for Industrial Science & Technology (ISTK) (KERI_14-12-N0101-13) and a National Research Foundation of Korea Grant funded by the Korean Government (MEST) (NRF-2013-C1AAA001-0030538).

REFERENCES

(1) Poizot, P.; Laruelle, S.; Grugeon, S.; Dupont, L.; Tarascon, J.-M. Nano-sized Transition-Metal Oxides as Negative-electrode Materials for Lithium-ion Batteries. *Nature* **2000**, *407*, 496−499.

(2) Green, M.; Fielder, E.; Scrosati, B.; Wachtler, M.; Moreno, J. S. Structured Silicon Anodes for Lithium Battery Applications. *Electrochem. Solid-State Lett.* **2003**, *6*, A75−A79.

(3) Tran, T. D.; Feikert, J. H.; Song, X.; Kinoshita, K. Commercial Carbonaceous Materials as Lithium Intercalation Anodes. *J. Electrochem. Soc.* **1995**, *142*, 3297−3302.

(4) Veeraraghavan, B.; Durairajan, A.; Haran, B.; Popov, B.; Guidottib, R. Study of Sn-Coated Graphite as Anode Material for Secondary Lithium Ion Batteries. *J. Electrochem. Soc.* **2002**, *149*, A675−A681.

(5) Peled, E.; Menachem, C.; Bar-Tow, D.; Melman, A. Improved Graphite Anode for Lithium-Ion Batteries Chemically Bonded Solid Electrolyte Interface and Nanochannel Formation. *J. Electrochem. Soc.* **1996**, *143*, L4−L7.

(6) Ortiza, G. F.; Hanzua, I.; Knauth, P.; Lavela, P.; Tirado, J. L.; Djenizian, T. TiO_2 Nanotubes Manufactured by Anodization of Ti thin films for On-chip Li-ion 2D Microbatteries. *Electrochim. Acta* **2009**, *54*, 4262−4268.

(7) Taberna, P. L.; Mitra, S.; Poizot, P.; Simon, P.; Tarascon, J.-M. High Rate Capabilities Fe3O4-based Cu Nano-architectured Electrodes for Lithium-ion Battery Applications. *Nat. Mater.* **2006**, *5*, 567−573.

(8) Xianjun, Z.; Zhu, Y.; Murali, S.; Stoller, M. D.; Ruoff, R. S. Nanostructured Reduced Graphene Oxide/Fe_2O_3 Composite As a

High-Performance Anode Material for Lithium Ion Batteries. *ACS Nano* **2011**, *5*, 3333−3338.
(9) Liu, J.; Dongfeng, X. Hollow Nanostructured Anode Materials for Li-Ion Batteries. *Nanoscale Res. Lett.* **2010**, *5*, 1525−1534.
(10) Lou, X. W.; Deng, D.; Lee, J. Y.; Feng, J.; Archer, L. A. Self supported formation of Needle like Co3O4 Nanotubes and their Application as Lithium-ion Battery Electrodes. *Adv. Mater.* **2008**, *20*, 258−262.
(11) Bruce, P. G.; Scrosati, B.; Tarascon, J.-M. Nanomaterials for Rechargeable Lithium Batteries. *Angew. Chem., Int. Ed.* **2008**, *47*, 2930−2946.
(12) Chen, J.; Xu, L.; Li, W.; Gou, X. α-Fe_2O_3 Nanotubes in Gas Sensor and Lithium-Ion Battery Applications. *Adv. Mater.* **2005**, *17*, 582−586.
(13) Jiang, J.; Li, Y. Y.; Liu, J. P.; Huang, X. T. Building One-Dimensional Oxide Nanostructure Arrays on Conductive Metal Substrates for Lithium-Ion Battery Anodes. *Nanoscale* **2011**, *3*, 45−58.
(14) Liu, J. P.; Li, Y. Y.; Fan, H. J.; Zhu, Z. H.; Jiang, J.; Ding, R. M.; Hu, Y. Y.; Huang, X. T. Iron Oxide-Based Nanotube Arrays Derived from Sacrificial Template-Accelerated Hydrolysis: Large-Area Design and Reversible Lithium Storage. *Chem. Mater.* **2010**, *22*, 212−217.
(15) Duan, H. N.; Gnanaraj, J.; Chen, X. P.; Li, B. Q.; Liang, J. Y. Fabrication and Characterization of Fe_3O_4-based Cu Nanostructured Electrode for Li-ion Battery. *J. Power Sources* **2008**, *185*, 512−518.
(16) Sue, K.; Sato, T.; Kawasaki, S. I.; Takebayashi, Y.; Yoda, S.; Furuya, T.; Hiaki, T. Continuous Hydrothermal Synthesis of Fe_2O_3 Nanoparticles Using a Central Collision-Type Micromixer for Rapid and Homogeneous Nucleation at 673 K and 30 MPa. *Ind. Eng. Chem. Res.* **2010**, *49*, 8841−8846.
(17) Li, J.; Xiong, S.; Liu, Y.; Ju, Z.; Qian, Y. High Electrochemical Performance of Monodisperse $NiCo_2O_4$ Mesoporous Microspheres as an Anode Material for Li-Ion Batteries. *ACS Appl. Mater. Interfaces* **2013**, *5*, 981−988.
(18) Muraliganth, T.; Murugan, A. V.; Manthiram, A. Facile Synthesis of Carbon-decorated Single-crystalline Fe_3O_4 Nanowires and Their Application as High Performance Anode in Lithium- Ion Batteries. *Chem. Commun.* **2009**, *87*, 7360−7362.
(19) Duan, L. H.; Huang, Y. D.; Jia, D. Z.; Wang, X. C.; Guo, Z. P. Fe_3O_4 Fuzzy Spheroids as Anode Materials for Lithium-ion Batteries. *Mater. Lett.* **2012**, *71*, 151−153.
(20) Roy, P.; Berger, S.; Schmuki, P. TiO_2 Nanotubes: Synthesis and Applications. *Angew. Chem., Int. Ed.* **2011**, *50*, 2904−2939.
(21) Cheng, H.; Lu, Z.; Ma, R.; Dong, Y.; Wang, H. E.; Xi, L.; Zheng, L.; Tsang, C. K.; Li, H.; Chung, C. Y.; Zapien, J. A.; Li, Y. Y. Rugated Porous Fe_3O_4 Thin Films as Stable Binder-free Anode Materials for Lithium Ion Batteries. *J. Mater. Chem.* **2012**, *22*, 22692−22698.
(22) Ortiz, G. F.; Hanzu, I.; Djenizian, T.; Lavela, P.; Tirado, J. L.; Knauth, P. Alternative Li-Ion Battery Electrode Based on Self-organized Titania Nanotubes. *Chem. Mater.* **2009**, *21*, 63−67.
(23) Ryu, W. H.; Nam, D. H.; Ko, Y. S.; Kim, R. H.; Kwon, H. S. Electrochemical Performance of a Smooth and Highly Ordered TiO_2 Nanotube Electrode for Li-ion Batteries. *Electrochim. Acta* **2012**, *61*, 19−24.
(24) Pervez, S. A.; Kim, D.; Sim, S.; Farooq, U.; Yaqub, A.; Hwang, M.; Choi, J. H.; Lee, Y. J.; Doh, C. H. Improved Performance of Ag-nanoparticle-decorated TiO_2 Nanotube Arrays in Li-Ion Batteries. *J. Korean Phys. Soc.* **2013**, *62*, 1809−1814.
(25) Li, H.; Martha, S. K.; Unocic, R. R.; Luo, H.; Dai, S.; Qu, J. High Cyclability of Ionic Liquid-produced TiO_2 Nanotube Arrays as an Anode Material for Lithium-ion Batteries. *J. Power Sources* **2012**, *218*, 88−92.
(26) Bi, Z.; Paranthaman, M. P.; Menchhofer, P. A.; Dehoff, R. R.; Bridges, C. A.; Chi, M.; Guo, B.; Sun, X.-G.; Dai, S. Self-organized Amorphous TiO_2 Nanotube Arrays on Porous Ti Foam for Rechargeable Lithium and Sodium Ion Batteries. *J. Power Sources* **2013**, *222*, 461−466.
(27) Hong, I.; Angelucci, M.; Verrelli, R.; Betti, M. G.; Panero, S.; Croce, F.; Mariani, C.; Scrosati, B.; Hassoun, J. Electrochemical Characteristics of Iron oxide Nanowires During Lithium-promoted Conversion Reaction. *J. Power Sources* **2014**, *256*, 133−136.
(28) Kim, H. S.; Piao, Y.; Kang, S. H.; Hyeon, T.; Sung, Y.-E. Uniform Hematite Nanocapsules Based on an Anode Material for Lithium Ion Batteries. *Electrochem. Commun.* **2010**, *12*, 382−385.
(29) Liu, J.; Li, Y.; Fan, H.; Zhu, Z.; Jiang, J.; Ding, R.; Hu, Y.; Huang, X. Iron Oxide-Based Nanotube Arrays Derived from Sacrificial Template-Accelerated Hydrolysis: Large-Area Design and Reversible Lithium Storage. *Chem. Mater.* **2010**, *22*, 212−217.
(30) Albu, S. P.; Ghicov, A.; Schmuki, P. High Aspect Ratio, Self-ordered Iron Oxide Nanopores Formed by Anodization of Fe in Ethylene Glycol/NH_4F Electrolytes. *Phys. Status Solidi RRL* **2009**, *3*, 64−66.
(31) Shin, Y.; Lee, S. Self-organized Regular Arrays of Anodic TiO_2 Nanotubes. *Nano Lett.* **2008**, *8*, 3171−3173.
(32) Masuda, H.; Fukuda, K. Ordered Metal Nanohole Arrays Made by a Two-Step Replication of Honeycomb Structures of Anodic Alumina. *Science* **1995**, *268*, 1466−1468.
(33) Mor, G. K.; Varghese, O. K.; Paulose, M.; Grimes, C. A. Transparent Highly Ordered TiO_2 Nanotube Arrays via Anodization of Titanium Thin Films. *Adv. Funct. Mater.* **2005**, *15*, 1291−1296.
(34) Kowalski, D.; Kim, D.; Schmuki, P. TiO_2 Nanotubes, Nanochannels and Mesosponge: Self-organized Formation and Applications. *Nano Today* **2013**, *8*, 235−264.
(35) Toby, B. H. EXPGUI, A Graphical User Interface for GSAS. *J. Appl. Crystallogr.* **2001**, *34*, 210−213.
(36) Xie, K. Y.; Li, J.; Lai, Y. Q.; Lu, W.; Zhang, Z. A.; Liu, Y. X.; Zhou, L. M.; Huang, H. T. Highly Ordered Iron Oxide Nanotube Arrays as Electrodes for Electrochemical Energy Storage. *Electrochem. Commun.* **2011**, *13*, 657−660.
(37) Albu, S. P.; Ghicov, A.; Aldabergenova, S.; Drechsel, P.; LeClere, D.; Thompson, G. E.; Macak, J. M.; Schmuki, P. Formation of Double-Walled TiO_2 Nanotubes and Robust Anatase Membranes. *Adv. Mater.* **2008**, *20*, 4135−4139.
(38) Albu, S. P.; Kim, D.; Schmuki, P. Growth of aligned TiO_2 Bamboo-type Nanotubes and Highly Ordered Nanolace. *Angew. Chem., Int. Ed.* **2008**, *47*, 1916−1919.
(39) Kim, D.; Ghicov, A.; Schmuki, P. TiO_2 Nanotube arrays: Elimination of Disordered top Layers ("nanograss") for Improved Photoconversion Efficiency in Dye-sensitized Solar Cells. *Electrochem. Commun.* **2008**, *10*, 1835−1838.
(40) Reddy, M. V.; Yu, T.; Sow, C. H.; Shen, Z. X.; Lim, C. T.; Rao, G. V. S.; Chowdari, B. V. R. α-Fe_2O_3 Nanoflakes as an Anode Material for Li-Ion Batteries. *Adv. Funct. Mater.* **2007**, *17*, 2792−2799.